CFD Simulation of Flow and Turbulence in a Slurry Bubble Column

Diana Matonis, Dimitri Gidaspow, and Mitra Bahary
Dept. of Chemical and Environmental Engineering, Illinois Institute of Technology, Chicago, IL 60616

To develop a predictive, experimentally verified computational fluid dynamic model for gas−liquid−solid flow, a 3-D transient computer code for the coupled Navier−Stokes equations for each phase was developed. The principal input into the model is the viscosity of the particulate phase, which was determined from a measurement of the random kinetic energy of the 800-micron glass beads and a Brookfield viscometer. The computed time-averaged particle velocities and concentrations agree with PIV measurements of velocities and concentrations, obtained using a combination of gamma-ray and X-ray densitometry, in a slurry bubble column, operated in the bubbly-coalesced fluidization regime with a continuous flow of water. Both the experiment and simulation show a downflow of particles in the center of the column, and an upflow near the walls, and a nearly uniform particle concentration. Normal and shear Reynolds stresses were constructed from the computed instantaneous particle velocities. The PIV measurement and the simulation produced similar nearly flat horizontal profiles of turbulent kinetic energy of particles.

Introduction

Fluidized beds are widely used industrially because the particles can be introduced into and out of the reactor as a fluid, and because of good heat and mass transfer in the reactor. For a conversion of synthesis gas (syngas) into methanol or hydrocarbon liquid fuels, a slurry bubble-column reactor has several advantages over a fixed-bed reactor (Bechtel Group, 1990; Viking Systems International, 1994). The cooling-surface requirement is less than in a fixed-bed reactor. Catalyst deactivation due to carbon formation can be handled by catalyst withdrawal and removal, whereas replacement of the fixed-bed catalyst requires a shutdown. In view of these advantages, slurry bubble-column reactors have recently (Parkinson, 1997) become competitive with fixed-bed reactors for converting syngas into liquid fuels. Fan (1989) has reviewed other applications of three-phase fluidization.

Slurry reactor design is usually done (Bechtel Group, 1999; Viking Systems International, 1994), using holdup correlations. In the early 1990s Tarmy and Coulaloglu (1992) of EXXON showed that there were no three-phase hydrodynamic models in the literature and that there was a need for such models, as illustrated by the development of a three-phase hydrodynamic model at EXXON that was presented at the 1996 Computational Fluid Dynamics in Reaction Engineering Conference (Heard et al., 1996). Today, computational fluid dynamics (CFD) has emerged as a new paradigm for modeling multiphase flow and fluidization, as seen from recent conferences (NICHE, 2000; FLUIDIZATION IX, 1998; CFD in Reaction Engineering, 2000), the formation of an industry-led, Department of Energy Multiphase Fluid Dynamics Research Consortium (Thompson, 1999), which consists of six national laboratories, six universities and American chemical companies, and papers published throughout the world. (The term CFD has come to denote minimal simulation using Navier−Stokes equations.)

Three types of CFD models are being used in literature to model gas−solid multiphase flow fluidization:

1. Viscosity input models, where the principal input is an empirical viscosity. Examples are the articles of Anderson, et al. (1995) for bubbling beds, Tsuo and Gidaspow (1990), and Benyahia et al. (1998) for risers.

Correspondence concerning this article should be addressed to D. Matonis.

2. Kinetic-theory-based models, as described in Gidaspow (1994). The most successful example of this model is the prediction of the core-annular regime by Sinclair and Jackson (1998) for steady developed flow in a riser. Transient simulations and comparisons to data were done by Samuelsberg and Hjertager (1996), Neri and Gidaspow (2000), and Mathiesen et al. (2000) for multisize flow.

3. K-Epsilon Model, where the K corresponds to the granular temperature equation and epsilon is a dissipation for which another conservation law is required. Its success has been to model turbulence for steady single-phase flow. It appears as an option in most commercial CFD codes. Kashiwa and VanderHeyden (1998) are extending this model to a multiphase flow as a part of the Multiphase Fluid Dynamics Consortium, where a discussion has begun at the quarterly meetings concerning mechanisms of turbulence production and dissipation.

In single-phase flow, the most fundamental approach to turbulence is direct numerical simulation (DSN) of the Navier–Stokes equations. It was quite successful in predicting the logarithmic velocity profile for channel flow (Kim et al., 1985) and other turbulence profiles, but with current computers and solution methods, is restricted to relatively low Reynolds numbers, about 10,000. The viscosity input model for multiphase flow is a method similar to the DNS in a single-phase flow. With particular input viscosities, a system of coupled Navier–Stokes equations is solved producing instantaneous fluctuating velocities. Averaging of these velocities

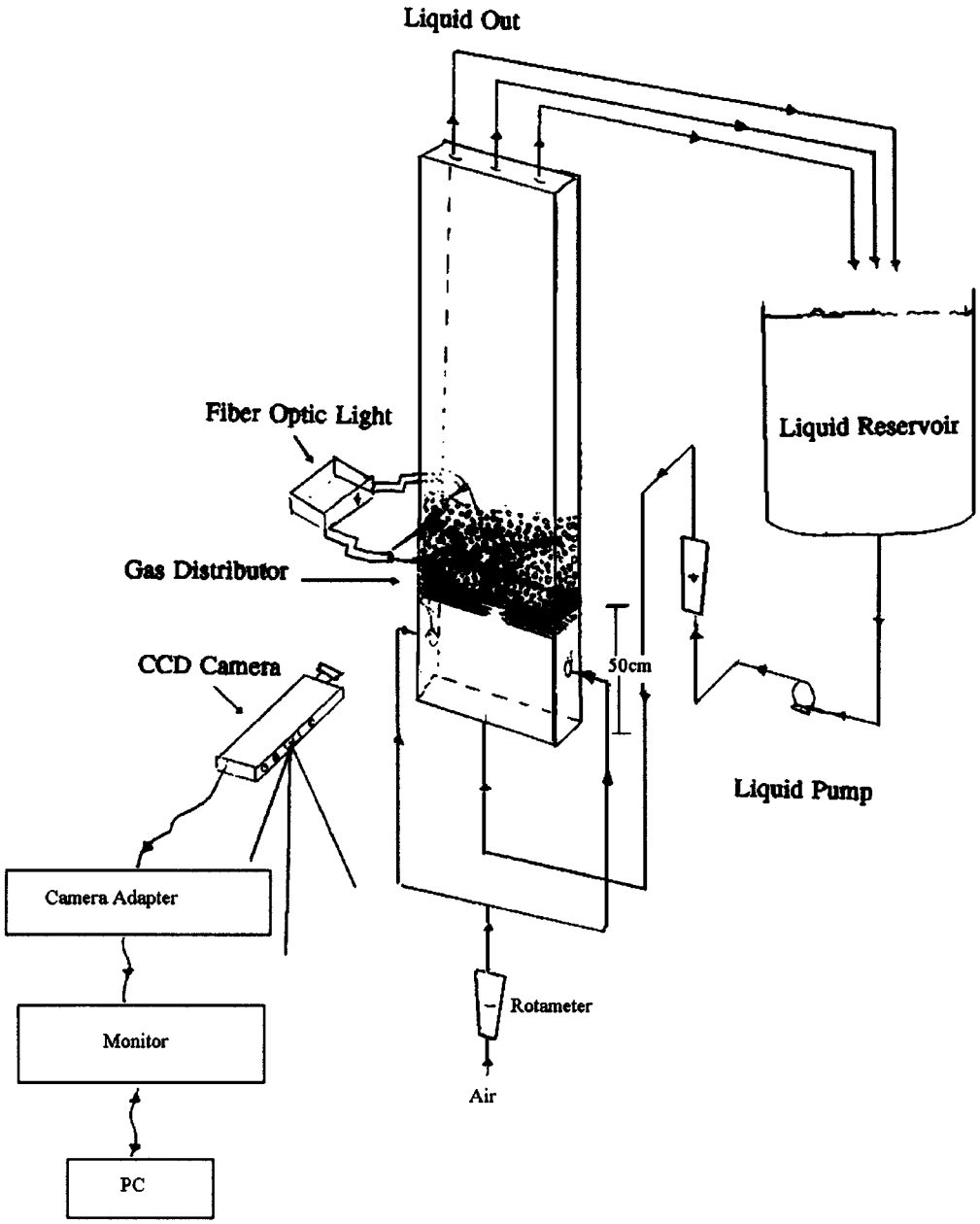

Figure 1. Three-phase fluidization system.

produces the normal and the shear Reynolds stresses for the various phases. Such a computation was recently done for a bubble column by Pan et al. (2000) using the Los Alamos CFDLIB code. Their comparison to the particle image velocity (PIV) data of Mudde et al. (1997) was quite good.

This article presents a similar computation for three phases. The computed time average particle gas and solids holdups, and the particle velocities generally agree with the measurements in a slurry bubble column. The computed horizontal profile of turbulent-particle kinetic energy also agrees with the PIV measurements, like those of Mudde et al. (1997).

Recently Pfleger et al. (1999) and Kishna et al. (1999) applied the commercial CFX code to bubble columns using the K-epsilon model, while Grevskott et al. (1996) successfully compared their computed steady-state velocity profiles to their experiments. Li et al. (1999) computed the bubble shape in the three-phase system by using an advection equation for the bubble surface. Discrete particle methods have also been used for simulating gas–solid systems (for example, Xu and Yu, 1997; Kwaguchi et al. 1998; Tsuji et al., 1998), but have not been applied to slurry bubble columns.

The experiments and the CDF computations presented in this article are in the so-called bubbly-coalesced flow regime, also called the churn-turbulent regime. Such a flow regime occurs in large-diameter columns for reasonably large input gas velocities, say 0.02 m/s. Much below this velocity one would be in the dispersed-bubble regime.

The large "bubbles" in the bubbly-coalesced regime are caused by the intersection of the paths of the fine bubbles. In the slurry bubble column, unlike in the bubble column without solids, these bubbles are not very distinct. They contain solids and almost disappear at high liquid velocities. Therefore, they are hard to characterize experimentally and have so far proved to be impossible to compute. The computations only show the ghosts of the bubbles, for example, high velocities in the region where a large bubble was expected. Figure 6.3 in Gadaspow's book (1994) is a picture of the most distinct bubbles that could be obtained in the experimental setup described here. These bubbles are for liquid velocities about half the speed of those analyzed in this article.

In the CFD simulation separate momentum balances are solved for the continuous flowing liquid phase and for the discrete solid and gas phases. The gas phase is treated as a particulate phase, as is the standard practice in the CFD simulation of gas–liquid bubble columns (for example, Pan et al., 2000). Since the flow inside the column is not far from homogeneous, one can add the three momentum equations and see that the total pressure is the sum of the individual phase pressures, and that the mixture viscosity is the sum of the three phase viscosities. The vicosity of the bubble gas phase and its collisional pressure are small, while the viscosity of the solid phase is large. Its measured value is used here.

Experimental Bubbly-Coalesced Flow Regime

Experimental Setup. The setup used in the bubbly-coalesced regime for volume fraction, velocity, and viscosity measurement experiments consisted of four major parts: fluidization equipment, densitometers assembly, a high-resolution microimaging I measuring system or a video–digital camera unit, and a Brookfield viscometer. The fluidized bed and

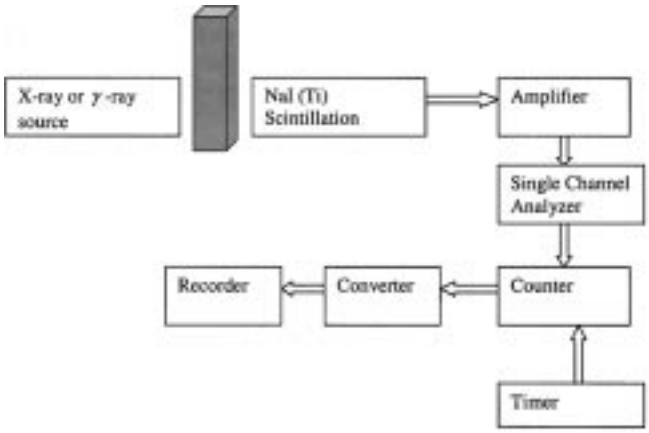

Figure 2. Source-detector-recorder assembly for X-ray and γ-ray densitometers.

video–digital camera unit for velocity measurements is shown in Figure 1. The source–detector–recorder assembly for X-ray and γ-ray densitometers for volume fraction measurements is shown in Figure 2.

Fluidization Equipment. A rectangular bed was constructed from transparent acrylic (Plexiglas) sheets to facilitate visual observation and video recording of the bed operations, such as gas bubbling and coalescence, and the mixing and segregation of solids. The bed height was 213.36 cm, and cross section was 30.48 cm by 5.08 cm. A centrifugal pump was connected to the bottom of the bed by a 1.0-in. (2.54-cm) diameter stainless-steel pipe. Gas injection nozzles from an air compressor were connected to the sides of the bed. Liquid was stored in and recycled back to a fifty-five gallon storage tank.

The liquid and gas distributors were located at the bottom of the bed. Two perforated Plexiglas plates with 0.28-cm-diameter holes distributed the liquid. They were located 35.6 cm and 50.8 cm above the bottom of the bed, and had 0.25-cm-size glass-bead particles inside. The gas distributor consisted of six staggered porous tubes of 15.24-cm length and 0.28-cm diameter. The fine pores of porous tubes had a mean diameter of 42 μm. The porous tubes were placed at the bottom of the bed, just below the top liquid distributor plate.

Densitometer Assembly. Two densitometers were used alternately for measuring the time-averaged volume fractions of the three phases at a designated location by means of the X-ray and γ-ray adsorption techniques. The assembly consisted of radioactive sources as well as detecting and recording devices and a positioning table. The source, detector, and recording devices assembly is shown in Figure 2.

Radioactive Source. A 200-mCi Cu-244 source having a 17.8-year half-life was used. It emitted X-rays with photon energy between 12 and 23 keV. The source was contained in ceramic enamel, recessed into a stainless-steel support with a tungsten alloy packing, and sealed in a welded Monel capsule. The device had a brazed beryllium window. For the γ-ray densitometer, a 20-mCi Cs-137 source having a single γ-ray of 667 keV and a half-life of 30 years was used. The source was sealed in a welded, stainless-steel capsule. The source holder was welded, filled with lead, and provided with a shut-

ter to turn off the source. This is the same unit used previously by Seo and Gidaspow (1987).

Detecting and Recording Devices. The intensity of the X-ray beam was measured by using a NaI crystal scintillation detector (Teledyne, ST-82-I/B). It consisted of a 2-mm-thick, 5.08-cm-diameter tube with 0.13-mm-thick beryllium window. For the γ-ray densitometer, the intensity of the γ-ray beam was detected by another NaI crystal detector (Teledyne, S-44-I/2). The crystal was 5.08 cm thick and 5.08 cm in diameter. The two detectors could be switched for use with different sources. The photomultiplier of the detector was connected sequentially to a preamplifier, an amplifier, and a single-channel analyzer, a rate meter, and a 186 IBM compatible personal computer. The rate meter has a selector and a 0–100-mV scale range.

Positioning Table. Both the source holder and detector were fastened to either side of the bed on a movable frame and could be moved anywhere up-or-down or side-to-side by means of an electric motor.

Particle Image Velocity System. The digital camera techniques used to measure particle velocities as shown on Figure 1 contained the following units:

1. *Image Recording and Displaying Devices*. A high-resolution color video camera, equipped with electronic shutter speed setting ranging from Off to 1/10,000 s and a superfine-pitch color monitor, were used to record and display solid velocities.

2. *Data Recording Device*. A 486 I 33-MHz IBM compatible personal computer with a microimaging board inside and microimaging software. Image-Pro Plus were used to record and store raw solid velocity data at any given location inside the fluidized bed.

Brookfield Viscometer. Brookfield digital viscometer (model LVDV-II+) with a spring torque of 673.7 dyne·cm was used to measure the effective bed viscosities. This viscometer can produce twenty different rotational speeds ranging from 0 to 100 revolutions per minute (rpm) at four different modes, namely, LV, RV, HA, and HBDV-II+.

Experimental procedure and interpretation

Fluidization Experiments. The liquid from the storage tank was fed to the bed from the bottom of the bed using the centrifugal pump. The gas was fed to the bed through a compressor. Both the gas and liquid from the top of the bed were directed through three openings of 1.0-in. (2.54-cm) diameter back to the storage tank, where the gas was separated from the liquid.

In order to achieve a uniform fluidization, the liquid distributor section was designed in such a way that the pressure drop through the distributor section was 10–20% of the total bed pressure drop. The gas was distributed in the fluidized bed through the six staggered porous tubes.

In this experiment, air and water were used as the gas and liquid, respectively Ballotini (leaded glass beads), with an average diameter of 0.889 cm and a density of 2.94 g/cm^3 were used as the solids. The experimental operating conditions are shown in Table 1 (Bahary, 1994).

Table 1. Operating Conditions for Bubbly-Coalesced Regime Experiments

Temperature (°C)	23.5
Particle mean diameter (cm)	0.8
Particle density (g/cm^3)	2.94
Initial bed height (cm)	22/24
Minimum fluidization velocity (cm/s)	0.76

Volume Fraction Determination. X-Ray and γ-ray densitometers have been used to measure porosities of fluidized beds (Miller and Gidaspow, 1992; Seo and Gidaspow, 1987; Gidaspow et al., 1995), and solids concentrations in nonaqueous suspensions (Jayaswal et al., 1990). These techniques are based on the fact that the liquid, gas, and solid phases under consideration have different absorptivities for X-ray and γ-rays. The same concept was adopted to measure concentration profiles inside our three-phase fluidization systems. The particles used in this system contain lead, to aid in the absorption of X-rays.

The intensity of the transmitted X-rays or γ-rays are described as a linear function of the volume fractions of liquid, gas, and the solid phases. The amount of radiation that is absorbed by a material can be given by the Beer–Bougert–Lambert law

$$I = I_o \exp(-\kappa \rho l) \tag{1}$$

where I is the intensity of transmitted radiation, I_o is the intensity of incident radiation, κ is the attenuation coefficient, ρ is the density of material, and l is the path length.

The logarithmic form of Eq. 1 for three-phase (gas–liquid–solid) fluidized beds is

$$-\ln\left[\frac{I}{I_o}\right] = A_g \epsilon_g + A_l \epsilon_l + A_s \epsilon_s \tag{2}$$

where

$$A = \kappa \rho l \tag{3}$$

and where I is the intensity readings of the X-ray or γ-ray densitometers, and ϵ_g, ϵ_l, and ϵ_s are the volume fractions of gas, liquid, and solid phases, respectively. The relation for the volume fractions is

$$\epsilon_g + \epsilon_l + \epsilon_s = 1.0 \tag{4}$$

The coefficients in Eq. 2 were calculated using the least-square error technique from the calibration measurements of the intensity reading of X-ray and γ-ray densitometers at known concentrations of gas, liquid, and solids in three-phase mixtures. However, these coefficients were found to have values with a 20% error for X-ray and a 2% error for γ-ray densitometers.

Velocity Measurements. In order to get a good microscopic visualization of the movement of particles, a fiber-optic light was reflected on the field of view in the front and back of the bed. The field of view in most experiments was a 2-cm × 2-cm area. As the particles were fluidized inside the bed, the camera with a 18–108-mm zoom lens and close-up focus, transferred its field of view to the monitor with streak lines. These

streak lines represented the space traveled by the particles in a given time interval specified on the camera. The images were then captured and digitized by a microimaging board and analyzed using Image-Pro Plus software. Radial and axial velocity measurements were conducted at different locations inside the bed. The velocity vector was calculated as

$$v_x = \frac{\Delta L}{\Delta t}\cos\alpha \tag{5}$$

$$v_y = \frac{\delta L}{\Delta t}\sin\alpha \tag{6}$$

where, ΔL is the distance traveled, α is the angle from horizontal, Δt is the inverse of shutter speed, and v_x and v_y are the vertical and horizontal velocity components, respectively.

Viscosity Measurements using Brookfield Viscometer. The viscometer was placed at the top of the fluidized bed, and secured over the bed's centerline. A cylindrical spindle (#1 LV) of 0.9421-cm diameter, 7.493-cm effective length, and overall height of 11.50 cm was used. The cylindrical spindle was attached to the bottom of the viscometer without the guard, and was lowered inside the fluidized bed by an extension wire until it was completely immersed in the mixture during the measurements.

The measurements in this experiment were made under LV mode at different speeds between 2 and 20 rpm. At each rotational speed, between 10 and 30 readings were taken. The calibration of the viscometer–spindle apparatus was done using Newtonian liquid, namely, water.

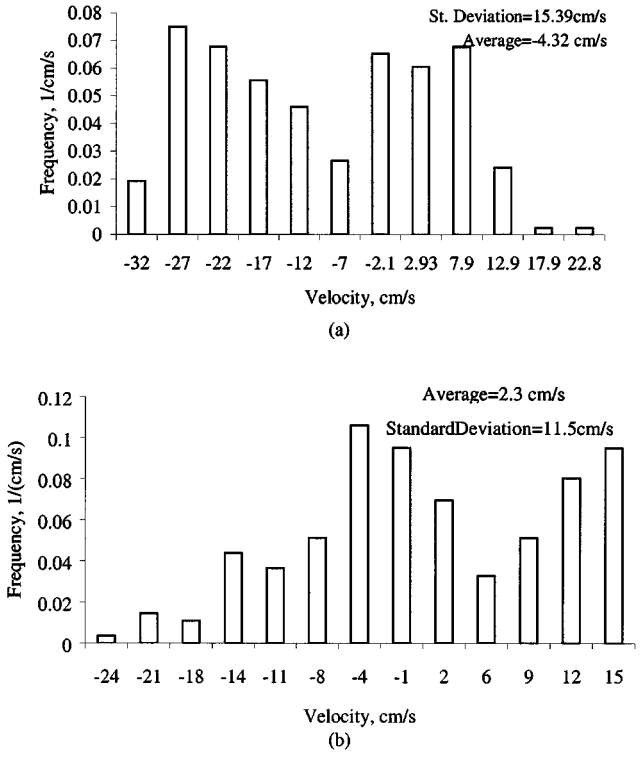

Figure 3. Experimental (a) vertical and (b) horizontal particle velocity distribution of solids at a bed height of 9 cm and horizontal position of 7.5 cm from left wall.

Table 2. Measured Phase Holdup in Bubble-Coalesced Regime for V_{gas} = 3.37 cm/s at 11 cm from the Left Wall

Bed heights, cm	2.5	5	7.5	10	12.5	15	17.5
ϵ_{solid}	0.25	0.18	0.15	0.16	0.2	0.25	0.2
ϵ_{air}	0.56	0.4	0.34	0.36	0.36	0.3	0.32

Granular Temperature Determination. The granular temperature, which is 3/2 of the random-particle kinetic energy, is obtained from the frequency distribution of the instantaneous velocities measured with the particle image velocity (PIV) system. Figure 3 shows typical distributions. The variances, σ^2, give the granular temperature, θ, as shown below

$$\theta = \frac{1}{3}\left[\sigma_x^2 + \sigma_y^2 + \sigma_z^2\right] \tag{7}$$

Since no distributions were measured into the depth of the bed, the z-direction, and since the variance in the direction of flow is the largest, in the calculation the assumption was made that the z-direction variance equals the x-direction variance. Hence

$$\theta = \frac{1}{3}\left[2\sigma_x^2 + \sigma_y^2\right] \tag{8}$$

Experimental results for bubbly-coalesced regime

Phase Holdup. From the calibration curves of the X-ray and γ-ray densitometers, the time-average values of the volume fraction for liquid, gas, and solid phases were calculated. Tables 2 and 3 contain such a subset of the volume fraction of gas and solids at varying heights and two different horizontal positions. The particle and gas concentrations appear to be nearly constant throughout the region. A computer simulation of this system, using an experimental superficial liquid velocity of 2 cm/s and gas velocity of 3.37 cm/s, also shows uniformity in the solids concentration distribution. Figure 4 compares the volume fractions obtained from the computer simulation with the experimental results. Computer simulations will be discussed in detail in the next section.

Instantaneous Velocity Distribution. The measured velocity data were analyzed using frequency distribution plots. The frequency distribution plots for particles' vertical and horizontal velocities are shown in Figures 3a and 3b for the three-phase fluidized bed.

Granular Temperature. Figure 5 shows a graph of the granular temperature, calculated using particle velocity measure-

Table 3. Measured Phase Holdup in Bubble-Coalesced Regime for V_{gas} = 3.37 cm/s at −2 cm from the Left Wall

Bed height, cm	2.5	5	7.5	10	12.5	15	17.5
ϵ_{solid}	0.15	0.21	0.08	0.12	0.1	0.15	0.16
ϵ_{air}	0.5	0.43	0.4	0.41	0.35	0.41	0.53

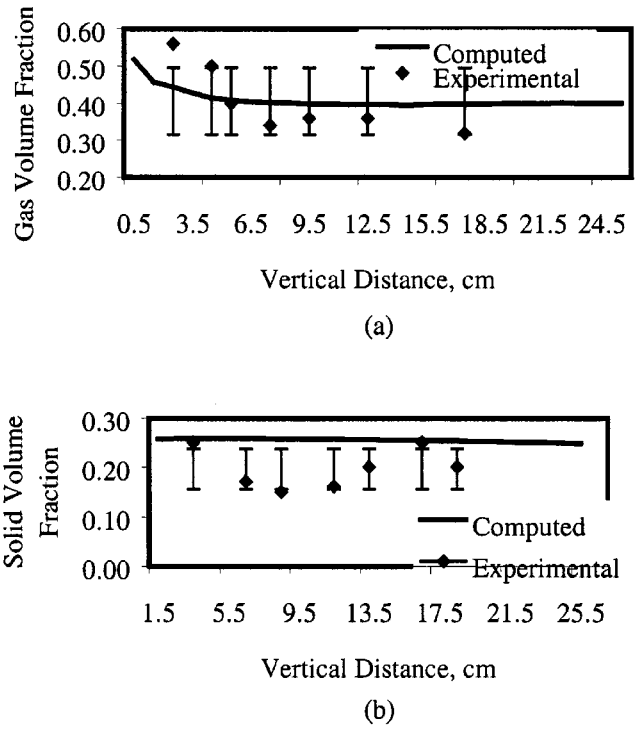

Figure 4. (a), (b) Comparison of measured and computed phase holdup in bubbly-coalesced regime for $V_L = 2.04$ cm/s and $V_G = 3.37$ cm/s at 4 cm from horizontal center of bed.

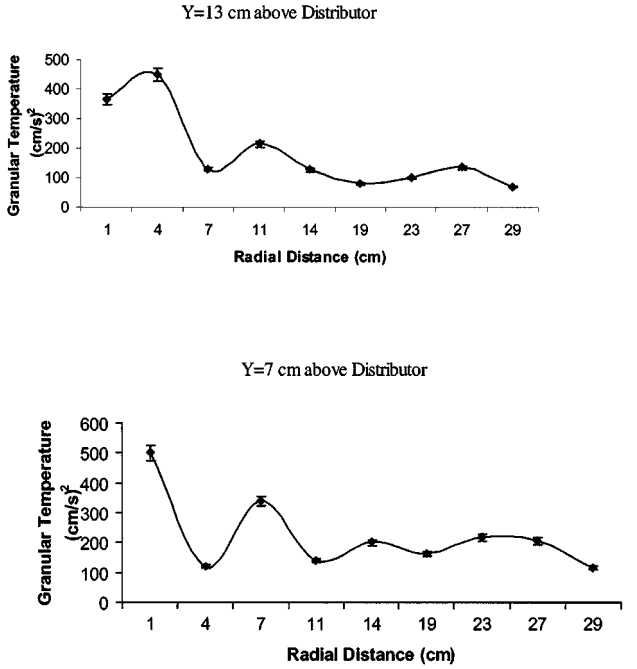

Figure 5. Granular temperature vs. horizontal distance from left wall at different bed heights in gas–liquid–solid fluidized bed at superficial liquid and gas velocities of 2.04 cm/s and 3.36 cm/s, respectively.

ments, as a function of horizontal distance from the centerline of the bed at two different heights. The granular temperature of the 800-micron beads is about 200 $(cm/s)^2$, except near the left wall, where there is a higher velocity and a more dilute flow due to the asymmetry in the system. This compares to about 1,000 $(cm/s)^2$ for 500-micron beads in air, determined in the IIT CFB, and about 10 $(cm/s)^2$ for 500-micron beads in water measured at IIT. Clearly, a higher gas flow increased the turbulence of the system. For 45-micron methanol catalyst particles, Wu and Gidaspow (2000) computed the granular temperature to be between 20 and 10 for volume fractions corresponding to 0.1 and 0.25, respectively. These computations approximately agree with the measurements of Mostofi (2002). The lower value of the granular temperature is due to the smaller particle size.

Fluid-Bed Viscosity. The viscosity of the glass beads in the mixture was obtained in two ways: (1) from a direct measurement of the viscosity by a Brookfield viscometer, and (2) from the measurement of the random particle velocity using the equation

$$\mu_s = \frac{5\rho_s d_s(\pi\theta)^{1/2}}{48(1+e)g_o}\left[1+\frac{4}{5}(1+e)g_o\epsilon_s\right]^2 + \frac{4}{5}(1+e)g_o\epsilon_s^2\rho_s d_s\left(\frac{\theta}{\pi}\right)^{1/2} \quad (9)$$

Gidaspow and Huilin (1996) have shown that these two methods give the same value of the viscosity for 75-micron FCC particles in a riser. The same result holds here, since the high viscosity of the 800-micron beads exceeds the viscosity of water and air. Figure 6 shows that the viscosities are the same within experimental error.

Simulation

Hydrodynamic model

A transient, isothermal, three-dimensional model for multiphase flow was developed (Matonis, 2000). The hydrodynamic model uses the principle of mass conservation and momentum balance for each phase. This approach is similar to that of Soo (1967) for multiphase flow, and of Jackson (1985) for fluidization. The equations are similar to Bowen's (1976) balance laws for multicomponent mixtures. The principal difference is the appearance of the volume fraction of phase

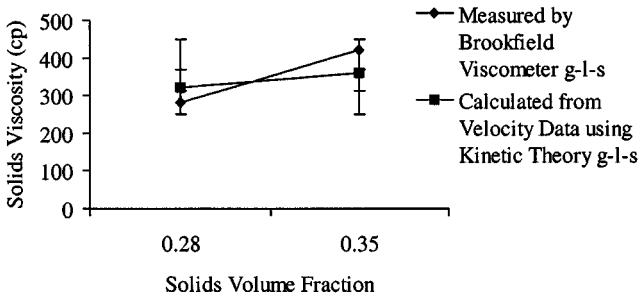

Figure 6. Experimental viscosities determined with a Brookfield viscometer and from measurement of random particle oscillations using PIV.

Table 4. Governing Equations

Continuity equation for each phase, $k = g,l,s$

$$\frac{\partial}{\partial t}(\epsilon_k \rho_k) + \nabla\cdot(\epsilon_k \rho_k \boldsymbol{v}_k) = 0$$

Continuous-phase (liquid) momentum balance

$$\frac{\partial}{\partial t}(\epsilon_f \rho_f \boldsymbol{v}_f) + \nabla\cdot(\epsilon_f \rho_f \boldsymbol{v}_f \boldsymbol{v}_f) = -\nabla\cdot P\bar{\bar{I}} + \rho_f g + \Sigma_{m=g,s}\beta_{fm}|\boldsymbol{v}_m - \boldsymbol{v}_f| + \nabla\cdot\bar{\bar{\tau}}_f$$

Dispersed-phase (gas or solid) momentum balance

$$\frac{\partial}{\partial t}(\epsilon_k \rho_k \boldsymbol{v}_k) + \nabla\cdot(\epsilon_k \rho_k \boldsymbol{v}_k \boldsymbol{v}_k) = -\nabla P_k \bar{I} + \frac{\epsilon_k}{\epsilon_f}(\rho_k - \Sigma_{m=f,g,s}\epsilon_m \rho_m)\boldsymbol{g} + \Sigma_{\substack{m=1,g,s \\ m\neq k}}\beta_{fm}|\boldsymbol{v}_m - \boldsymbol{v}_k| + \nabla\cdot\bar{\bar{\tau}}_k$$

Viscous stress tensor

$$[\bar{\bar{\tau}}_f] = 2\epsilon_k \mu_k[\bar{\bar{S}}_f]$$

$$[\bar{\bar{S}}_f] = \frac{1}{2}[\nabla\boldsymbol{v}_f + (\nabla\boldsymbol{v}_f)^T] - \frac{1}{3}[\nabla\cdot\boldsymbol{v}_f\bar{\bar{I}}]$$

"k" denoted by ϵ_k. The fluid pressure, P, is in the liquid (continuous) phase.

For gas–solid fluidized beds, Bouillard et al. (1989) have shown that this set of equations produces essentially the same numerical answers for fluidization as did the earlier conditionally stable model, which has the fluid pressure in both the gas and the solids phases. In this model (hydrodynamic model B), the drag and the stress relations were altered to satisfy Archimedes' buoyancy principle and Darcy's law, as illustrated by Jayaswal (1991). Note in Table 4, no volume fraction is put into the liquid gravity term, while the gas–solid system momentum balance contains the buoyancy term. This is a generalization of model B for gas–solid systems, as discussed by Gidaspow (1994, section 2.4). This model is unconditionally well posed, that is, the characteristics are real and distinct for a one-dimensional transient flow. The presence of the solids pressure for stability and well-posedness is not required.

The numerical method is an extension of Harlow and Amsden's (1971) method, which was subsequently used in the K-FIX program (Rivard and Torrey, 1977). The present program was developed from Jayaswal's (1991) two-dimensional MICE program, which originated from the K-FIX program (Rivard and Torrey, 1977). To obtain the numerical solution, a nonuniform computational mesh is used in finite-differencing the equations based on the ICE algorithm, implicit Eulerian method (Rivard and Torrey, 1977; Jayaswal, 1991), with appropriate initial and boundary conditions. Stewart and Wedroff (1984) have critically reviewed the ICE algorithm, and related conservative staggered mesh schemes. The scalar variables are located at the cell center and the vector variables at the cell boundaries. The momentum equation is solved using a staggered mesh, while the continuity equation is solved using a donor-cell method.

Table 4 shows the continuity and the separate phase-momentum equations for three-dimensional transient three-phase flow. There are nine nonlinear-coupled partial differential equations for nine dependent variables. The variables to be computed are the volume fractions, $\epsilon_{\text{phases}-1}$, the liquid-phase pressure, P, and the phase horizontal, x-direction, and vertical velocity, y-direction components, u_{phase} and v_{phase}. The gradient of pressure is in the fluid (continuous) phase only. This leads to an unconditionally well-posed problem, as discussed in detail by Gidaspow (1994) and Lyczkowski et al. (1978).

A value of 10 poises times the particle concentration was used throughout the simulations. This equation was obtained by fitting the experimental viscosity values at the given superficial liquid and gas velocities (Bahary, 1994). Therefore, the viscous stress terms for the phases are of the Newtonian form as follows

$$[\bar{\bar{\tau}}_k] = 2\epsilon_k \mu_k[\bar{\bar{S}}_k]; \qquad \mu_k = \epsilon_k 10(\text{poises})$$

$$[\bar{\bar{S}}_k] = \frac{1}{2}[\nabla\boldsymbol{v}_k + (\nabla\boldsymbol{v}_k)^T] - \frac{1}{3}[\nabla\cdot\boldsymbol{v}_k\bar{\bar{I}}] \quad (10)$$

The solids pressure is calculated by the solids stress modulus using the following equations

$$\nabla P_k = G(\epsilon_k)\nabla\epsilon_k; \qquad G(\epsilon_k) = 10^{-8.686\epsilon_k + 6.385}. \quad (11)$$

As a particle moves through a viscous liquid, there exists a resistance of the liquid to the motion of the particle, hence the interphase drag has to be defined. One type is the packed-pressure drop data expressed in the form of a correlation, such as the Ergun equation.

For $\epsilon_k \geq 0.2$

$$\beta_{fk} = \beta_{kf} = 150\frac{(1-\epsilon_f)\epsilon_k \mu_f}{(\epsilon_f d_k \psi_k)^2} + 1.75\frac{\epsilon_k \rho_f}{\epsilon} \quad (12a)$$

For $\epsilon_k < 0.2$, the empirical correlation is based on Stokes' drag coefficient C_d, as follows

$$\beta_{fk} = \beta_{kf} = \frac{3}{4}C_D\frac{\epsilon_k \epsilon_f^{-2.65}\rho_f}{d_k \psi_k}|\boldsymbol{v}_f - \boldsymbol{v}_k| \quad (12b)$$

where

$$C_D = \frac{24}{Re_k}\left[1 + 0.15Re_k^{0.687}\right], \quad \text{for } Re_k < 1{,}000$$

$$C_D = 0.44, \quad \text{for } Re_k \geq 1{,}000$$

Arastoopour et al. (1980) observed that solid–solid momentum transfer is necessary to correctly predict the segregation among particles of different sizes in a pneumatic conveyor. Particle–particle drag equations to describe such interactions have been derived by several researchers: Soo (1967), Nakamura and Capes (1976), and Syamlal (1985). In the present work the drag coefficient is based on kinetic theory (Syamlal, 1985) represented as

$$\beta_{\substack{kl \\ k\neq l}} = \frac{\alpha(1+e)\epsilon_k \rho_k \epsilon_l \rho_l (d_k + d_l)^2\left[1 + 3\left(\frac{\zeta_{kl}}{\epsilon_k + \epsilon_l}\right)^{1/3}\right]}{2\epsilon_f(\rho_k d_k^3 + \rho_l d_l^3)\left[3\left(\frac{\zeta_{kl}}{\epsilon_k + \epsilon_l}\right)^{1/3} - 1\right]} \quad (13)$$

where

$$\zeta_{kl} = \begin{cases} \left[(\phi_k - \phi_l) + (1-\alpha)(1-\phi_k)\phi_l\right]\left[\phi_k + (1-\phi_l)\phi_k\right]\dfrac{\chi_k}{\phi_k} + \phi_l & \text{for } \chi_k \le \dfrac{\phi_k}{\left[\phi_k + (1-\phi_k)\phi\right]} \\ (1-\alpha)\left[\phi_k + (1-\phi_k)\phi_l\right](1-\chi_k) + \phi_k & \text{for } \chi_k > \dfrac{\phi_k}{\left[\phi_k + (1-\phi_k)\phi_l\right]} \end{cases} \tag{14}$$

$$\alpha = \sqrt{\frac{d_l}{d_k}}, \quad d_k \ge d_l$$

$$\chi_k = \frac{\epsilon_k}{\epsilon_k + \epsilon_f}, \quad e = 0.9999$$

The gas phase is treated as a particulate phase by specifying the injected air-bubble diameter, viscosity, and density as visually seen in the experiment. The simulation results are time-averaged as follows

$$\langle v(x,y,z)\rangle = \frac{1}{t_o}\int_t^{t+t_o} v(y,z,t)\, dt \tag{15}$$

The other corresponding equations used to analyze the output from the simulation are summarized in Table 5. These equations are a result from time-averaging the equations of continuity and of motion (Bird et al., 1960). These terms are the components of the turbulent momentum flux and are referred to as the Reynolds stresses.

Coordinate system and numerical considerations

The solution of the preceding conservation equations depends on the definition of the boundary conditions for an adequate comparison to experiment. The diameter of the leaded glass beads was 0.899 cm with a density of 2.49 g/cm^3. The viscosity was an input in all simulations to match experimentally obtained viscosities, as discussed previously. Different inlet conditions and grid sizes were prescribed to test the sensitivity of the final flow-field solution and are summarized

Table 5. Equations of the Calculated Stresses

$$\langle v'v'\rangle = \left[\frac{1}{N(t)}\Sigma v(x,y,z,t)v(x,y,z,t)\right] - (\langle v(x,y,z)\rangle)^2$$

$$\langle u'v'\rangle = \langle v'u'\rangle = \frac{1}{N(t)}\Sigma[\{u(x,y,z,t) - \langle u(x,y,z)\rangle\}\{v(x,y,z,t) - \langle v(x,y,z)\rangle\}]$$

$$\langle u'u'\rangle = \left[\frac{1}{N(i)}\Sigma u(x,y,z,t)u(x,y,z,t)\right] - (\langle u(x,y,z)\rangle)^2$$

$$\langle u'w'\rangle = \langle w'u'\rangle = \frac{1}{N(t)}\Sigma[\{u(x,y,z,t) - \langle u(x,y,z)\rangle\}\{w(x,y,z,t) - \langle w(x,y,z)\rangle\}]$$

$$\langle w'w'\rangle = \left[\frac{1}{N(i)}\Sigma w(x,y,z,t)w(x,y,z,t)\right] - (\langle w(x,y,z)\rangle)^2$$

$$\langle v'w'\rangle = \langle w'v'\rangle = \frac{1}{N(t)}\Sigma[\{v(x,y,z) - \langle v(x,y,z)\rangle\}\{w(x,y,z) - \langle w(x,y,z)\rangle\}]$$

with $N(t)$ being the number of vectors in the time average

Table 6. Simulation Cases Under Investigation

Case	Δx, cm	Δy, cm	V_{Liquid} cm/s	V_{gas} cm/s	D_{air} cm	$\epsilon_{\text{left,water}}$	$\epsilon_{\text{left,gas}}$	$\epsilon_{\text{right,water}} = \epsilon_{\text{right,gas}}$
FB2d3d	15* 2	18* 5.825	8.074	6.078	0.1	0.6	0.4	0.5
FB1	32×1 cm	2* 2.25, 19* 4.5	4.04	3.37	0.01	0.5	0.5	0.5
FB2	32×1	31×1, 2,3,4,10×5	4.04	3.37	0.01	0.5	0.5	0.5
FB3	14×2.5	2* 2.25, 19* 4.5	4.04	3.37	0.01	0.5	0.5	0.5
FB4	14∗2.5	2* 2.25, 19* 4.5	4.04	3.37	0.1	0.5	0.5	0.5
FB5	15* 2.03 2	18* 5.623	4.04	3.37	0.1	0.6	0.4	0.5

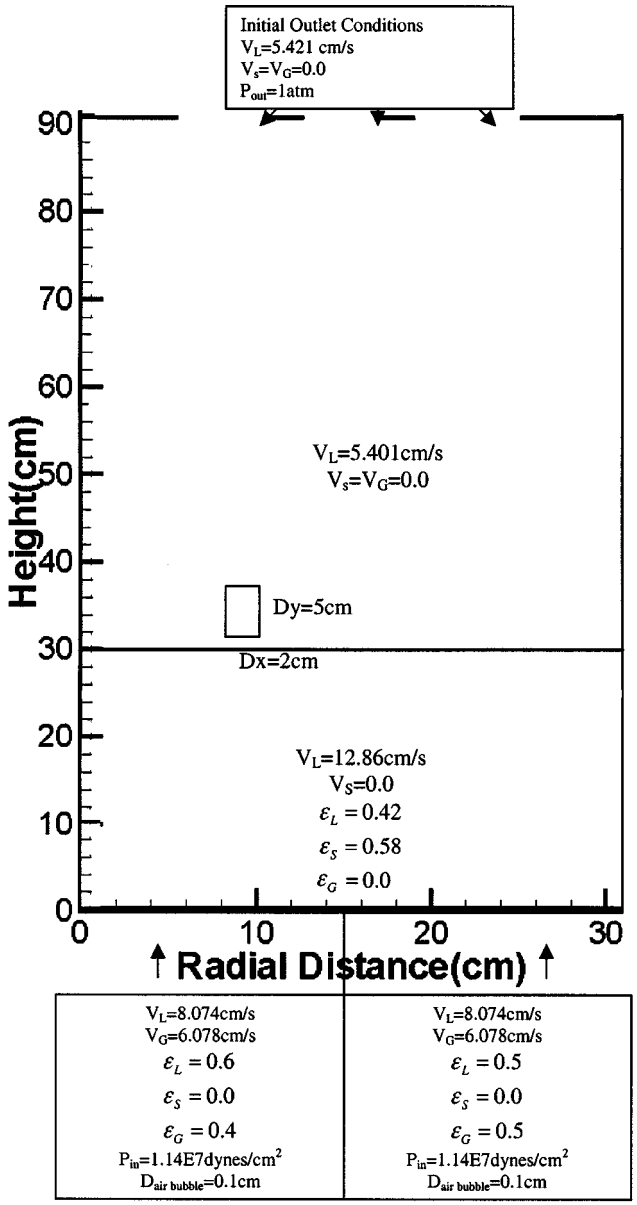

Figure 7. Inlet and initial conditions for simulations.

as cases in Table 6. Figure 7 illustrates the two-dimensional computational domain for case FB2d3d in Table 6. The third dimension, to represent the experimental 5.08-cm depth of the bed, is added with a grid size of 1.02 cm. It will be shown that the two-dimensional simulation can properly represent the flow hydrodynamics and be less computer time intensive. The remainder of this section will study the effects of varying grid size, injected air-bubble diameter, and void fraction as represented in Table 6. The left side represents the inlet from the left wall to the centerline of the horizontal, 15 cm.

Three-dimensional simulation: Case FB2d3d in Table 6

Flow Field and Averaged Velocity Profiles. Figures 8a and 8b show the three-dimensional time-averaged, 16- to 42-s gas and solid volume fraction contour plots along with the time-averaged velocity vectors at the *x-y* plane, 3 cm from the front wall. Figure 8c shows the solid contour plot with corresponding velocity vectors at a time of 39 s in the *y-z* plane, 17.5 cm from the left wall. The computed flow pattern correctly shows gas upflow in the center region, as visually confirmed in the experiment. A video of the experiment and of the simulations shows that the solid fluctuates upward and downward in the center region. Time-averaged velocities show the solid moving downward in the center, as illustrated in Figure 8b. The phenomenon of downward flow of particles in the center is almost identical to that observed experimentally in a two-dimensional gas–solid fluidized bed at low gas velocities, where the bubbles form between the center of the bed and the walls, as shown in figure 10.5b in Gidaspow's (1994) book. His figure 10.5a shows the corresponding computations. His vorticity equation (Eq. 10.46) explains the phenomenon quantitatively. Once bubbles form near the walls, producing an upward motion of particles in this region, conservation of the mass of particles forces them to descend in the center.

Figure 9 shows that the two-dimensional time-averaged vertical velocities overlap the three-dimensional time-averaged velocity pattern, and both agree well with the experiment. Figure 10 further illustrates that the solids vertical velocity does not change when going into the bed. Figure 11 further demonstrates the time-averaged water downward vertical velocities in the center region. This downflow in the center produces a rotation or particle vorticity, as seen in Figure 8a. Due to the buoyancy, air moves up only.

Reynolds Stresses. The stresses are calculated from the velocity vectors directly using equations presented in Table 5. The profiles of Figures 12 and 13 and all cases studied show that the Reynolds stress $\langle u'u' \rangle$ peaks in the center, whereas $\langle v'v' \rangle$ peaks close to the walls, in agreement with Muddle et al. (1997) and Pan et al. (2000), for gas–liquid flow only. The explanation of the appearance and diagonal vortical movement by Muddle et al. (1997) causes drastic swings in the vertical velocity close to the wall, where the motion is primarily upward. The horizontal velocity attains its highest magnitude in the center, contributing the most to the horizontal stresses in the center, but the least by the wall. At the left wall, the vertical Reynolds stress is the highest, thus the granular temperature exhibits this maximum at the wall, as shown in Figure 14. From experiment (Figure 5), the same characteristic experimental maximum turbulence is observed closer to the left wall, even at the lower inlet water and air superficial velocities. Figure 13 shows the stresses plotted into the depth at an *z-y* plane of 12 cm from the left wall. The horizontal stress exhibits the characteristic maximum in the center region, but the vertical Reynolds stress is much flatter. This can be attributed to the fact that there is no vortex formation in the third direction.

Two-dimensional low-velocity simulations

Flow Field and Averaged Velocity Profiles. Figure 15 represents the time-averaged, 15- to 44-s, solid contour plot and velocity vectors for Case FB5. Figure 16a illustrates the time-averaged solids contour plot and velocity vectors for Case FB2. The only difference between these two cases is the

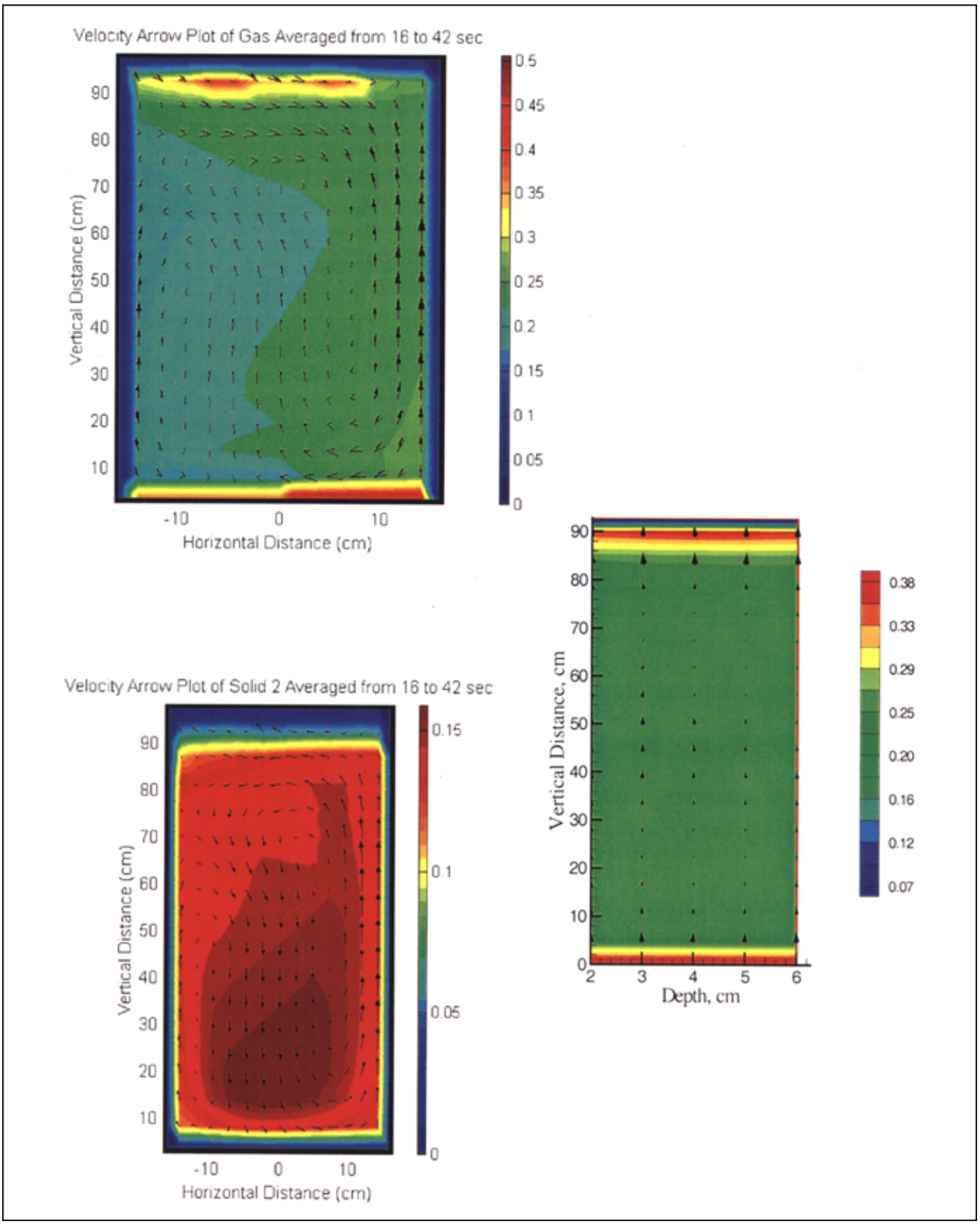

Figure 8. Time-averaged volume fractions and velocities (a) [top, left] for gas, (b) [bottom, center] for particles, and (c) 3 cm from front wall [right] for particles.

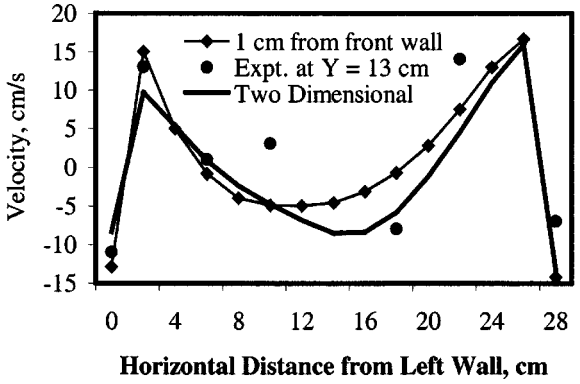

Figure 9. A comparison of 2-D and 3-D vertical particle velocities to PIV measurements.

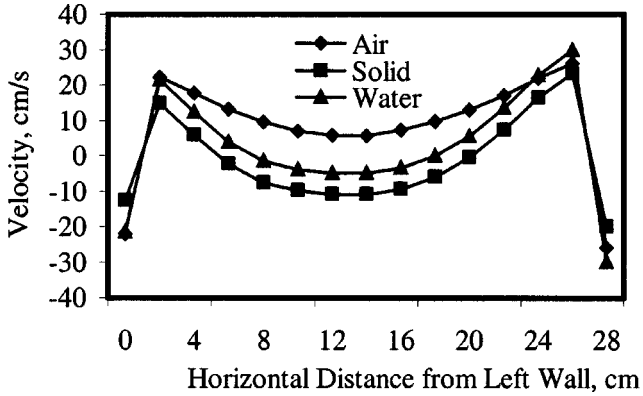

Figure 11. Comparison of time-averaged vertical velocities for gas, particles, and liquid at the center of the vessel.

injected air bubble diameter and grid size. From Figures 17 through 19 it can be seen that grid size did not affect the transient behavior of the bed. Figures 15 and 16a show that the difference in the bed expansion is due to the increase in bubble diameter. Figures 16b–16c illustrate the instantaneous vortex movement from 14 s to 15 s for Case FB2.

Figure 20 shows the power spectrum of the vertical velocity for Case FB2 at 8 cm from the left wall and at a bed height of 11 cm. Muddle et al. (1997) had found a similar low-frequency peak and no dominant frequency above 1 Hz, and Bahary (1995) has measured similar low frequencies. The time-averaged vertical and horizontal velocities are presented in Figure 17 and agree with the experimental averages, Figure 3, of 2.3 cm/s for the vertical velocity and -4.32 cm/s for the horizontal velocity at a bed height of 9 cm and horizontal position of 7.5 cm from the left wall. Figures 17, 18, and 19 represent the time-averaged velocities for the remaining cases with an injected air-bubble diameter of 0.01 cm. The agreement of the time-averaged velocities of Figures 17, 18, and 19 is expected, since the grid size is the only thing that varies between these cases. However, a noticeable difference exists in these figures and Figures 21 and 22. Figure 21 represents the time-averaged horizontal and vertical particle-velocity profiles for a uniform inlet with only an inlet bubble diameter increase. These profiles are much flatter due to the lack of vortical structure production. Figure 22 represents the larger injected air-bubble diameter and not symmetric inlet conditions (Case FB5). This velocity plot is not flat; instead, there exists an increase in the velocity in the half of the bed where more gas is injected.

Reynolds Stresses and Granular Temperature. Figures 23, 24, and 25 show how damping of the stresses occurs by an increase in grid size. From Figure 23 to 24, the *y*-directional grid cell is halved in size from 2.5/4.5 cm to 1 cm. The shape of the curves remains the same, but the stresses are doubled. The same pattern can be seen when going from Figure 25 to Figure 23, where the *x*-directional grid cell is halved in length and the stresses are doubled in size. Thus, the stresses appear to be linearly proportional to the grid size and are due to the small calculated stress values for this three-phase system. However, this grid-size dependency is not seen with the granular temperature.

The granular temperature is compared to the experiment in Figure 26, and shows general agreement. The damping in the stresses can also be seen in the granular temperature; as the mean fluctuation of the velocity decreases, so does the granular temperature. Figure 27 represents the granular temperature of the larger inlet bubble diameter (Case FB4), and as the time-averaged velocity profile was flattened, so was the granular temperature. The test for developed flow, as in DNS for a single phase, was performed in these cases. Figure 28 shows the test for the developed flow of case FB3.

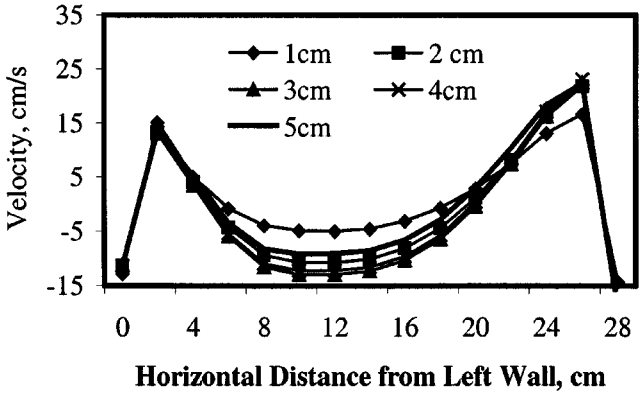

Figure 10. Time-averaged vertical particle velocities for various depths from front plate.

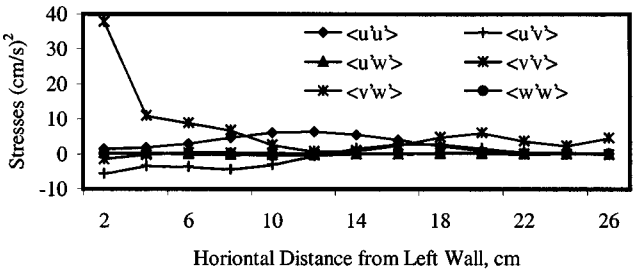

Figure 12. Typical computed Reynolds stresses for particles at a bed height of 11.3 cm.

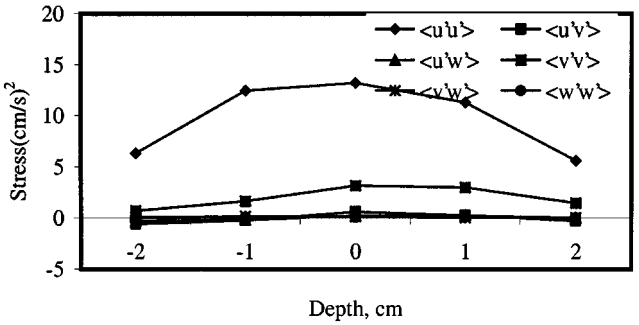

Figure 13. Variation of Reynolds stresses with depth at a bed height of 11.3 cm and 12 cm from left wall.

The following equations are used to obtain curves

$$\int -\frac{dP}{dy} - g \sum_{i=1}^{3} (\epsilon_i \rho_i)\, dx$$

= pressure drop minus weight of bed

$$\langle u' v' \rangle \sum_{i=1}^{3} (\epsilon_i \rho_i) = \text{principal Reynolds stress} \qquad (16)$$

The two expressions are not equal, because the u and v velocities (see Figure 8) are of the same order of magnitude due to the vortex formation. The stresses shown in Figure 28 are on the order of magnitude of the solid's pressure, which is approximately equal to

$$P_s = \epsilon_s \rho_s v_s^2 \qquad (17)$$

This value is small as compared to the fluid pressure.

Discussion

Computations of the granular temperature and frequency allow us to speculate concerning vortex size from dimensional analysis, and approximate solutions of Navier–Stokes equations for standing waves (Tolstoy, 1973). Characteristic

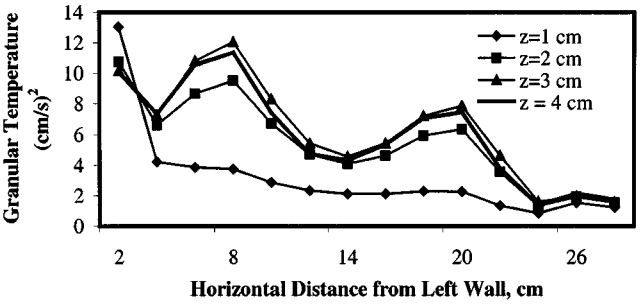

Figure 14. Granular temperature (3/2 particle random kinetic energy) at several bed depths.

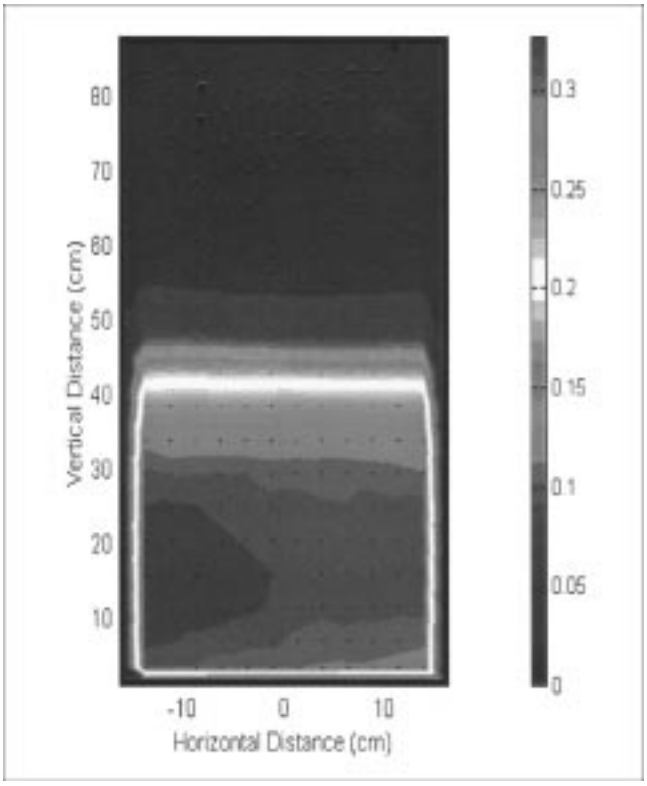

Figure 15. Particle contour and velocity vector plot for Case FB5.

length equals the pseudosonic velocity divided by the major frequency, where the pseudosonic velocity equals the square root of the granular temperature. From Figure 26 we see that the granular temperature ranges between 50 and 100, and the major frequency is taken to be 0.3 Hz. Entering these ranges into the equation gives us vortex sizes of 20 and 30 cm. Hence, in our system, we expect to have one to two vortices and do not expect any vortices into the depth of the bed. Figure 8 shows that there is no vortex in the third dimension. Figures 16b–16d better illustrate the instantaneous single and double vortices generated by the code, and which are also seen in the experiment. This fluctuating particle vorticity and the flow of the liquid cause the particle concentration to be uniform throughout the bed. This is in contrast with the case of no liquid flow, where there is a vertical density gradient (Wu and Gidaspow, 2000). Such a catalyst distribution is reasonable. It is usually modeled using a sedimentation model (Viking, 1993). In the production of gasoline in an FCC riser, there exists a sharp radial catalyst gradient. In view of this undesirable distribution of particles, other designs such as the downer are being considered. Hence, the discovery of a uniform concentration described in this study is of some practical significance. In the future, this model will be explored further. In addition, its principal weakness is in the uncertainty of the bubble size. Figures 15 and 16 show an order-of-magnitude difference in the bed expansion caused by the order-of-magnitude increase in the inlet bubble diameter. Such an effect is reasonable, since the bed expands a lot more for fine particles or fine bubbles.

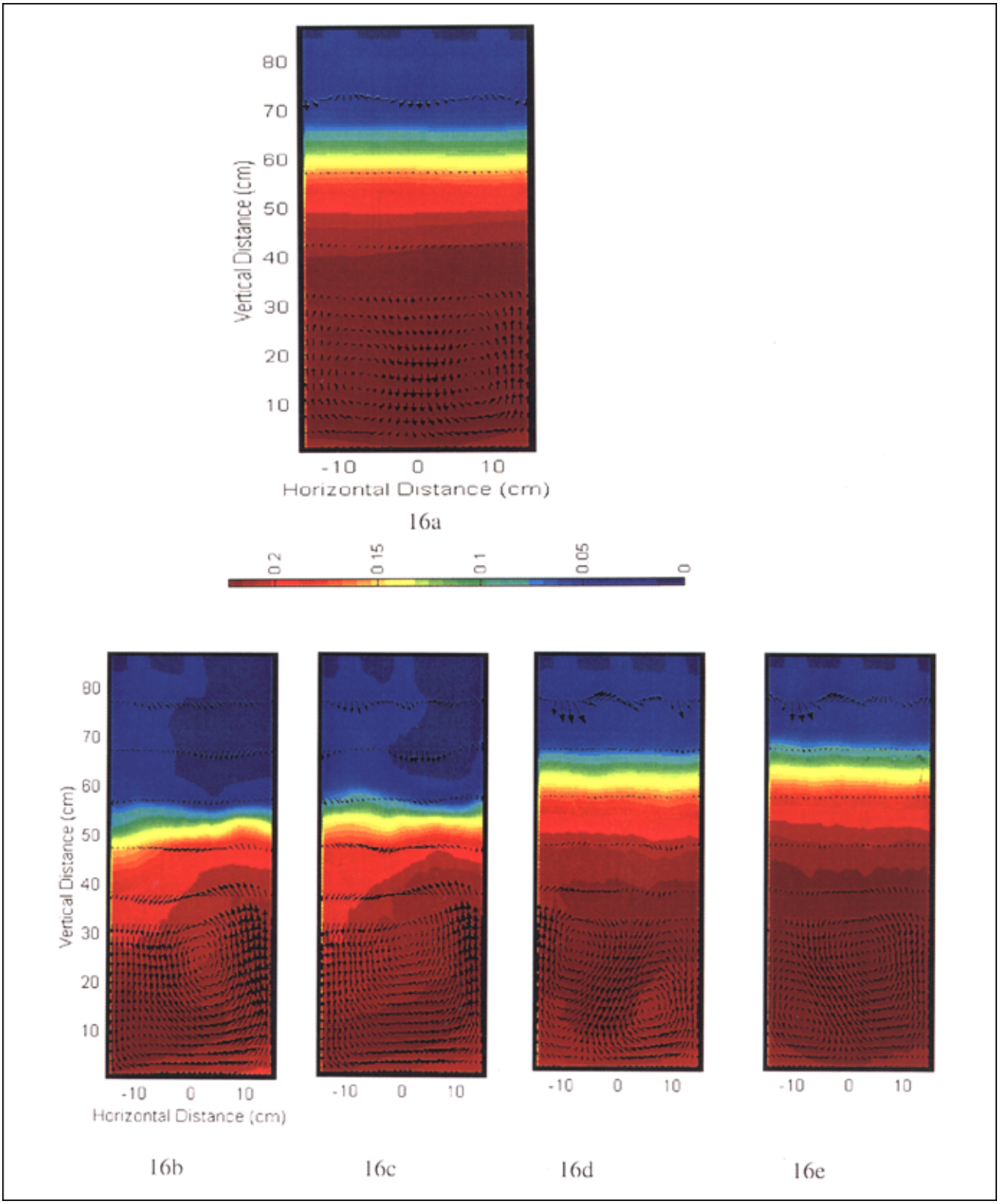

Figure 16. (a) Time-averaged and instantaneous time, (b) 14 s, (c) 15 s, (d) 25 s, (e) 28 s volume fraction contour and velocity vector for Case FB2 with the corresponding color map bar for volume fractions values.

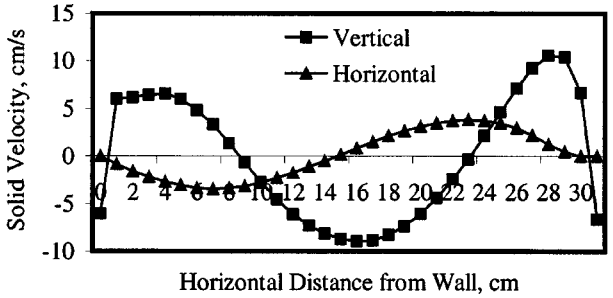

Figure 17. Time-averaged vertical and horizontal particle velocities for Case FB2 at a bed height of 9 cm.

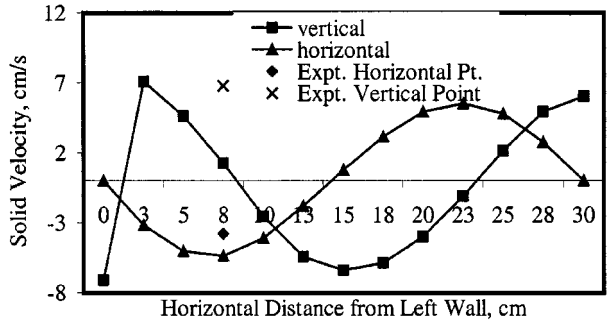

Figure 18. Time-averaged vertical and horizontal particle velocities for Case FB3 at a bed height of 9 cm.

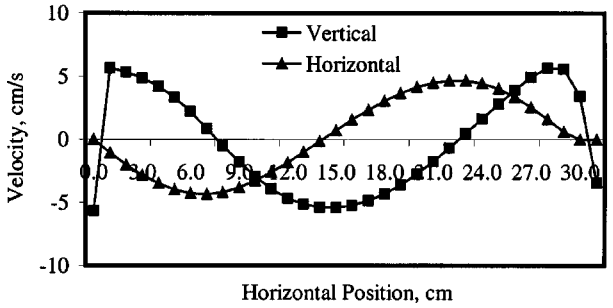

Figure 19. Time-averaged vertical and horizontal particle velocities for Case FB1 at a bed height of 9 cm.

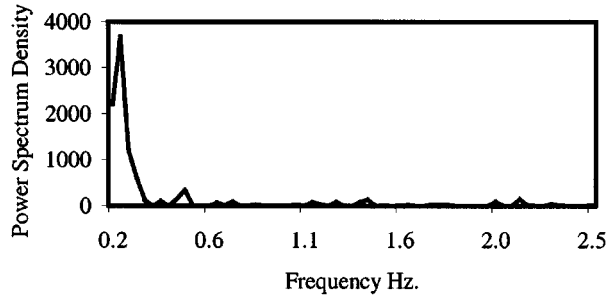

Figure 20. Power spectrum of the solid axial velocity profile for Case FB2.

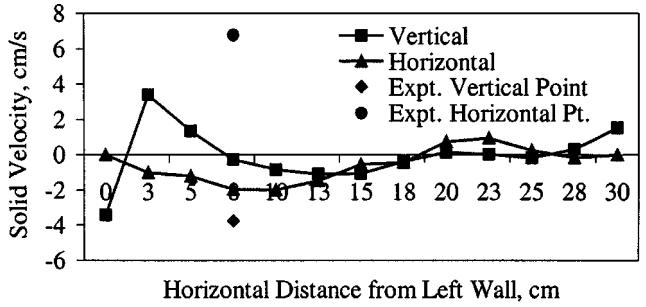

Figure 21. Time-averaged vertical and horizontal particle velocities for Case FB4 at a bed height of 9 cm.

Conclusions

1. A transient, three-dimensional computer code for the solutions of the coupled Navier–Stokes equations for gas–liquid–solid flow was developed. The principal input is the particulate viscosity, which was measured with a Brookfield viscometer and a PIV technique.

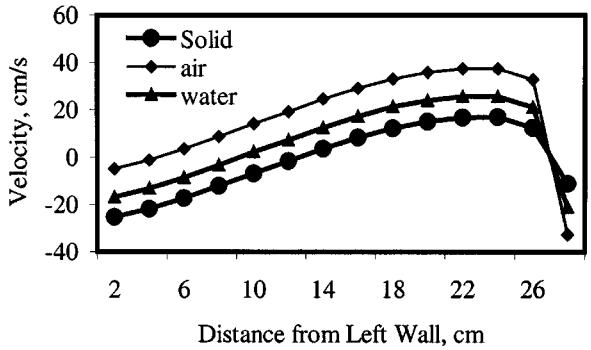

Figure 22. Time-averaged vertical and horizontal particle velocities for Case FB5 at a bed height of 9 cm.

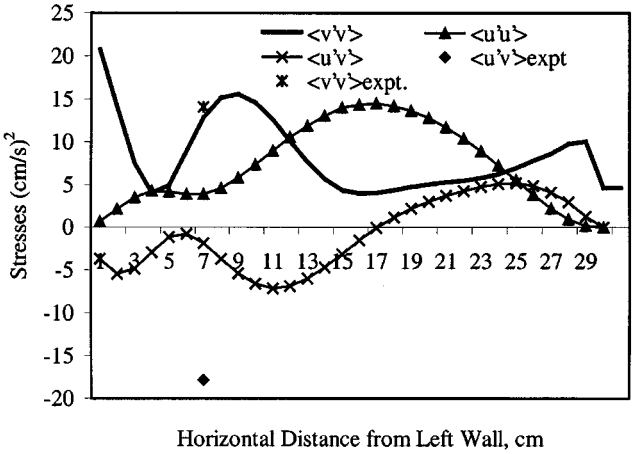

Figure 23. Comparison of computed normal and Reynolds shear stresses for Case FB1 and experimental points at a bed height of 9 cm.

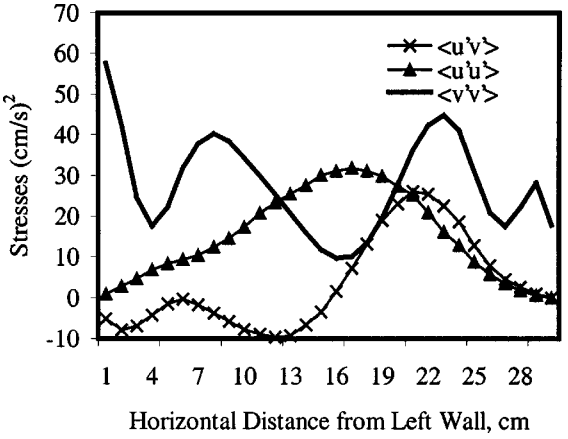

Figure 24. Comparison of computed normal and Reynolds shear stresses for Case FB2 at a bed height of 9 cm.

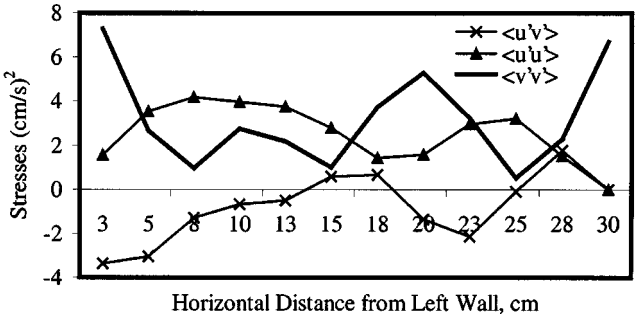

Figure 25. Comparison of computed normal and Reynolds shear stresses for Case FB3 and experimental points at a bed height of 9 cm.

2. The computed time-average particle velocities and concentrations agree with measurements done in the slurry bubble column with the continuous flow of liquid in the churn-turbulent regime. The particle velocities were measured using the PIV technique. The concentrations were determined using a combination of γ-ray and X-ray densitomers. Both the experiment and the simulations show a downflow of particles in the center of the column with the upflow near the wall. The situation is unlike the case of no liquid recirculation (Wu and Gidaspow, 2000), where there exist large inhomogeneities of particles in the bed.

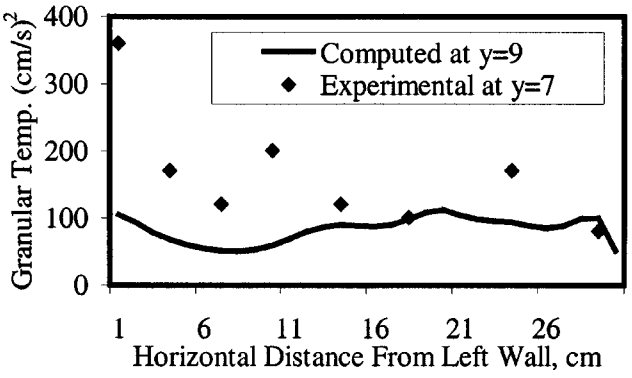

Figure 26. Comparison of computed (Case FB2) and experimental granular temperature points at a bed height of 9 cm.

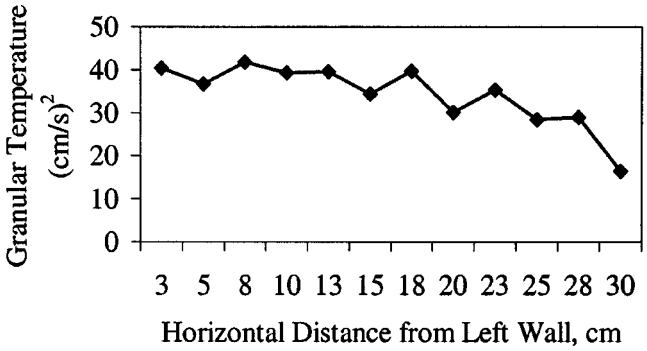

Figure 27. Comparison of computed (Case FB4) granular temperature at a bed height of 9 cm.

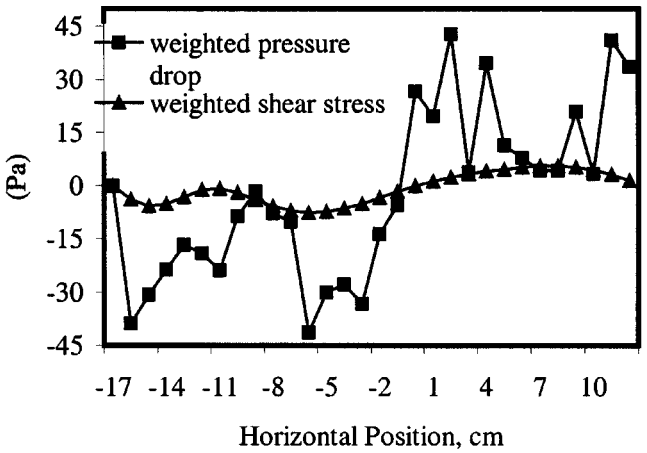

Figure 28. Test for developed flow for case FB3.

3. Computed instantaneous particle velocities were used to construct normal and shear Reynolds stresses, similar to the procedure in DNS for single-phase flow. The computed horizontal distributions of granular temperature, the turbulent kinetic energy of particles, agreed with measurements done using a PIV technique.

Acknowledgments

This study was partially supported by Department of Energy Grant No. DE-PS26-98FT98200 and NSF Grant 0086250.

Notation

C_D = drag coefficient
d_k = characteristic particulate phase diameter
e = coefficient of restitution
g = gravity
G = solid compressive stress modulus
g_o = radial distribution function at contact
P = continuous-phase pressure

P_k = dispersed (particulate) phase pressure
Re_k = Reynolds number for phase k
t = time
u = horizontal velocity, x-direction
v = vertical velocity, y-direction
w = depth velocity, z-direction

Greek letters

β_{km} = interphase momentum transfer coefficient between k and m
ϵ_k = volume fraction of phase k
θ = granular temperature
μ = viscosity
ρ = density
τ_k = stress
ϕ_k = solids volume fraction at maximum packing
Ψ = particle sphericity

Literature Cited

Anderson, K., S. Sundaresan, and R. Jackson, "Instabilities and the Formation of Bubbles in Fluidized Beds," *J. Fluid Mech.*, **303**, 327 (1995).

Arastoopour, H., D. Lin, and D. Gidaspow, "Hydrodynamic Analysis of Pneumatic Transport of a Mixture of Two Particle Sizes," *Multiphase Transport*, Vol. 4, T. N. Veziroglu, ed., Hemisphere, New York, p. 1853 (1980).

Bahary, M., "Experimental and Computational Studies of Hydrodynamics in Three-Phase and Two-Phase Fluidized Beds," PhD Thesis, Illinois Institute of Technology, Chicago (1994).

Bechtel Group, "Slurry Reactor Design Studies. Slurry vs. Fixed Bed Reactors For Fischer-Tropsch and Methanol: Final Report," No. DE91005752 (1990).

Benyahia, S., H. Arastoopour, and T. Knowlton, "Prediction of Solid and Gas Flow Behavior in a Riser Using a Computational Multiphase Flow Approach," *Fluidization X, Proc. Engineering Foundation Conf. on Fluidization*, L.-S. Fan and T. Knowlton, eds., New York (1998).

Bird, R. B., W. E. Stewart, and E. N. Lightfoot, *Transport Phenomena*, Wiley, New York (1960).

Bouillard, J. X., and D. Gidaspow, "Porosity Distribution in a Fluidized Bed with an Immersed Obstacle," *AIChE J.*, **35**, 908 (1989).

Bowen, R. M., *Theory of Mixtures*, Continuum Physics, Vol. III, A. C. Eringen, ed., Acedemic Press, New York (1976).

Fan, L.-S., *Gas Liquid-Solid Fluidization Engineering*, Butterworths, Boston (1989).

Gidaspow, D., *Multiphase Flow and Fluidization: Continuum and Kinetic Theory Descriptions*, Academic Press, New York (1994).

Gidaspow, D., M. Bahary, and Y. Wu, "Hydrodynamic Models for Slurry Bubble Column Reactors," *Proc. Coal Liquefaction and Gas Conversion Contractors Review Conf.*, DOE/PETC, p. 397 (1995).

Gidaspow, D., and L. Huilin, "Collisional Viscosity of FCC Particles in a CFB," *AIChE J.*, **42**, 2503 (1996).

Grevskott, S., B. H. Sannaes, M. P. Dudukovic, K. W. Hjarbo, and H. F. Svendsen, "Liquid Circulation, Bubble Size Distributions and Solid Movement in Two- and Three-Phase Bubble Columns," *Chem. Eng. Sci.*, **51**, 1703 (1996).

Harlow, F. H., and A. Amdsen, "A Numerical Fluid Dynamics Calculation Method for all Flow Speeds," *J. Comput. Phys.*, **8**, 197 (1971).

Heard, W. B., and G. R. Richter, "Numerical Multiphase, Multicomponent Flow Modeling," Computational Fluid Dynamics in Chemical Reaction Engineering, United Engineering Foundation, San Diego (1996).

Jackson, R., "Hydrodynamic Stability of Fluid-Particle Systems," *Fluidization*, J. F. Davidson, R. Cliff, and D. Harrison, eds., Academic Press, New York, p. 47 (1985).

Jayaswal, U. K., "Hydrodynamics of Multiphase Flows: Separation, Dissemination and Fluidization," PhD Thesis, Illinois Institute of Technology, Chicago (1991).

Kashiwa, B. A., and W. B. VanderHeyden, "An Extended K-Epsilon Turbulence Model for Multiphase Flow," *U.S. National Congress of Applied Mechanics*, Univ. of Florida, Gainesville, FL (1998).

Kim, J., P. Moin, and R. Moser, "Turbulence Statistics in Fully Developed Channel Flow at Low Reynolds Number," *J. Fluid Mech.*, **177**, 133 (1987).

Krishna, R., M. I. Urseanu, J. M. Van Baten, and J. Ellenberger, "Influence of Scale on the Hydrodynamics of Bubble Columns Operating in the Churn-Turbulent Regime: Experiments vs. Eulerian Simulations," *Chem. Eng. Sci.*, **54**, 4903 (1999).

Kwaguchi, K., T. Tanaka, and Y. Tsuji, "Numerical Simulation of Two-Dimensional Fluidized Beds Using the Discrete Element Method (Comparison Between the Two- and Three-Dimensional Models)," *Powder Technol.*, **96**, 129 (1998).

Li, Y., J. Zhang, and L.-S. Fan, "Numerical Simulation of Gas-Liquid-Solid Fluidization Systems Using a Combined CFD-VOF-DPM Method: Bubble Wake Behavior," *Chem. Eng. Sci.*, **54**, 5101 (1999).

Lyczkowski, R. W., D. Gidaspow, C. W. Solbrig, and E. C. Hughes, "Characteristics and Stability Analysis of Transient One-Dimensional Two-Phase Flow Equations and Their Finite Difference Approximations," *Nucl. Sci. Eng.*, **66**, 378 (1978).

Mathiesen, V., T. Solberg, H. Arastoopour, and B. Hjertager, "Experimental and Computational Study of Multiphase Gas/Particle Flow in a CFB Riser," *AIChE J.*, **45**, 2503 (1998).

Matonis, D., "Hydrodynamic Simulation of a Gas-Liquid-Solid Fluidization Bed," PhD Thesis, Illinois Institute of Technology, Chicago (2000).

Miller, A., and D. Gidaspow, "Dense, Vertical Gas-Solid Flow in a Pipe," *AIChE J.*, **38**, 1801 (1992).

Mostafi, "CFD Simulations of Particulate Two-Phase and Three-Phase Flows," PhD Thesis, Illinois Institute of Technology, Chicago (2002).

Muddle, R. F., D. J. Lee, J. Reese, and L.-S. Fan, "Role of Coherent Structures on Reynolds Stresses in a 2-D Bubble Column," *AIChE J.*, **43**, 913 (1997).

Nakamura, K., and C. E. Capes, "Vertical Pneumatic Conveying of Binary Particle Mixtures," *Fluidization Technology*, Vol. II, New York (1976).

Neri, A., and D. Gidaspow, "Riser Hydrodynamics: Simulation Using Kinetic Theory," *AIChE J.*, **46**, 52 (2000).

NICHE, The Council for Chemical Research New Industrial Chemistry and Engineering, "Conputational Chemistry and Fluid Dynamics," Marco Island, FL (2000).

Pan, Y., M. P. Dudukovic, and M. Chang, "Numerical Investigation of Gas-Driven Flow in 2-D Bubble Columns," *AIChE J.*, **46**, 434 (2000).

Parkinson, G., "Fischer-Tropsh Comes Back," *Chem. Eng.,* **104**, 39 (1997).

Pfleger, D., S. Gomes, N. Gilbert, and H.-G. Wagner, "Hydrodynamic Simulations of Laboratory Scale Bubble Columns Fundamental Studies of Eulerian-Eulerian Modeling Approach," *Chem. Eng. Sci.*, **54**, 5091 (1999).

Rivard, W. C., and M. D. Torrey, "K-FIX: A Computer Program for Transient Two-Dimensional, Two-Fluid Flow," LA-NUREG-6623, Los Alamos, NM (1977).

Samuelsberg, A., and B. H. Hjertager, "Computational Modeling of Gas/Particle in a Riser," *AIChE J.*, **42**, 1536 (1996).

Seo, Y., and D. Gidaspow, "An X-Ray-Gamma-Ray of Measurement of Binary Solids Concentrations and Void in Fluidized Beds," *Ind. Eng. Chem. Res.*, **26**, 1622 (1987).

Sinclair, J. L., and R. Jackson, "Gas-Particle Flow in a Vertical Pipe with Particle-Particle Interactions," *AIChE J.*, **35**, 1473 (1989).

Soo, S. L., *Fluid Dynamics of Multiphase Systems*, Blaisdell, Waltham, MA (1967).

Stewart, H. B., and B. Wendroff, "Two-Phase Flow: Models and Methods," *J. Comput. Phys.*, **56**, 363 (1984).

Symlal, M., "Multiphase Hydrodynamics of Gas-Solid Flow," PhD Thesis, Illinois Institute of Technology, Chicago (1985).

Tarmy, B. L., and C. A. Coulaloglou, "Alpha-Omega and Beyond Industrial View of Gas/Liquid/Solid Reactor Development," *Chem. Eng. Sci.*, **47**, 3231 (1992).

Thompson, T., "The Multiphase Fluid Dynamics Research Consortium," see "Vision 2020 Comes into Focus," *C&EN News* (1999).

Tolstoy, I., *Wave Propagation*, McGraw-Hill, New York (1973).

Tsuo, Y. P., and D. Gidaspow, "Computations of Flow Patterns in Circulating Fluidized Beds," *AIChE J.*, **36**, 885 (1990).

Tsuji, Y., T. Tanaka, and S. Yonemura, "Cluster Patterns in Circulating Fluidized Beds Predicted by Numerical Simulation (Discrete Particle Model versus Two-Fluid Model)," *Powder Technol.*, **95**, 254 (1998).
Viking System International, "Design of Slurry Reactor for Indirect Liquefaction Applications," Report to DOE/PETC by A. Parakash and P. B. Bendale, DE-AC22-89PC89870 (1994).
Wu, Y., and D. Gidaspow, "Hydrodynamic Simulation of Methanol Synthesis in Gas-Liquid Slurry Bubble Column Reactors," *Chem. Eng. Sci.*, **55**, 573 (2000).
Xu, B. H., and A. B. Yu, "Numerical Simulation of the GAS-Solid Flow in a Fluidized Bed by Combining Discrete Particle Method with Computational Fluid Dynamics," *Chem. Eng. Sci.*, **52**, 2785 (1997).

Manuscript received Aug. 7, 2000, and revision received Jan. 2, 2002.